

# Development of a thermo-mechanically coupled crystal plasticity modeling framework: application to polycrystalline homogenization

Jifeng Li<sup>a,b</sup>, Ignacio Romero<sup>a,c</sup>, Javier Segurado<sup>a,b,\*</sup>

<sup>a</sup>*IMDEA Materials Institute, Eric Kandel 2, Getafe, 28906 Madrid, Spain*

<sup>b</sup>*E.T.S. de Ingenieros de Caminos, Universidad Politécnica de Madrid, 28040 Madrid, Spain*

<sup>c</sup>*ETSI Industriales, Jose Gutierrez Abascal 2, Universidad Politécnica de Madrid, 28006 Madrid, Spain*

---

## Abstract

Accurate predictions of thermo-mechanically coupled process in metals can lead to a reduction of cost and an increase of productivity in manufacturing processes such as forming. For modeling these coupled processes with the finite element method, accurate descriptions of both the mechanical and the thermal responses of the material, as well as their interaction, are needed. Conventional material modeling employs empirical macroscopic constitutive relations but does not account for the actual thermo-mechanical mechanisms occurring at the microscopic level. However, the consideration of the latter might be crucial to obtain accurate predictions and a complete understanding of the underlying physics.

In this work we describe a fully coupled implicit thermo-mechanical framework for crystal plasticity simulations. This framework includes thermal strains, temperature dependency of the crystal behavior and heat generation by dissipation due to plastic slip and allows the use of large deformation steps thanks to the implicit integration of the governing equations. Its use within computational homogenization simulations allows to bridge the plastic deformation and temperature gradients at the macroscopic scale with the microscopic slip at the grain scale. A series of numerical examples are presented to validate the approach.

*Keywords:* Thermo-mechanical coupling, Crystal plasticity, Polycrystal homogenization, finite elements.

---

## 1. Introduction

Metallic materials usually undergo large plastic deformation under a wide range of strain rates and temperatures during forming and other manufacturing

---

\*Corresponding author. E-mail: javier.segurado@imdea.org(Javier Segurado)

processes. Accurate predictions of the material behavior in these situations are of great interest for industry since they are helpful for reducing the manufacturing cost and increasing the productivity. The response of metals in these processes is, however, very complex since their mechanical behavior is often strongly coupled with thermal phenomena. For example, the thermal variations may produce non-negligible effects on the mechanical behavior as the result of thermal expansion and/or contraction. Also, temperature changes may modify significantly the mechanical behavior of a material introducing softening, increasing its rate sensitivity, and may even cause phase transformations. On the other hand, the mechanical processes influence the thermal field via heat generation caused by plastic work dissipation, as well as through changes in the thermal boundary conditions due to the geometrical evolution of the material configuration. Thus, accurate simulations of those thermo-mechanical processes require a fully coupled modeling framework that can describe with precision both the mechanical and the thermal behaviors of the material, as well as their interaction.

The solution of a thermo-mechanical problem involves the consideration of the balance of momentum and balance of energy equations. Both of them are standard for small and large strain solid mechanics, but the material response to mechanical and thermal loading is very complex, more so if their coupling is considered. Given those difficulties, the thermo-mechanical response of metals is often modeled with phenomenological models such as Johnson-Cook's [1], Zerilli-Armstrong [2], and the Mechanical Threshold stress model [3]. These constitutive relations, and others employed in simulations, consciously ignore microscopic phenomena that take place at the sub-grain level, even when it is widely acknowledged that are precisely these which determine the mechanical behavior.

In order to develop models that can provide a higher degree of accuracy in their predictions it is mandatory to incorporate into them information regarding the microscopic behavior of the material. In particular, it has been observed experimentally that polycrystalline metals exhibit a marked anisotropic response during plastic deformation, and it is mainly caused by the crystallographic texture resulting from the reorientation of the grains. Hence, incorporating the evolution of texture in a detailed constitutive relation for the thermo-mechanical behavior of metallic polycrystals is absolutely required.

To this end, crystal plasticity (CP) was developed in the late 70s and 80s [4, 5, 6, 7] as a constitutive equation into the framework of continuum mechanics, based on the model envisioned by Taylor in the 30s. CP models predict the mechanical behavior of a single crystalline metal taking into account the dislocation slip through the slip planes characteristic of its lattice. The use of CP models within homogenization frameworks allows to simulate the response of a full polycrystal including texture evolution by explicitly considering grain orientation and shape changes in the micro-scale (see [8] for a review). Such type of models, due to their verified predictive capacity, have been used in the prediction of the mechanical response under monotonic loading [9, 10, 11, 12, 13, 14, 15], cyclic loading [16, 17, 18] and fatigue response [19, 20, 21, 22, 23] or to simulate

forming processes such as rolling [24, 25, 26, 27].

Temperature effects on the mechanical response of a polycrystal using computational models with realistic microstructures have been introduced in many studies [28, 29, 30, 31] using a standard, purely mechanical framework, neglecting the effect of thermal strains and not considering heat generation by plastic dissipation. The structural heating due to plastic dissipation in crystal plasticity has been accounted for as responsible for the *local* temperature increase using a Taylor model to homogenize the polycrystal response [32, 33]. Under the Taylor approach, individual grain orientations are considered, therefore accounting for the effect of texture. On the other hand, the state of each grain is represented by a single value for each field variable and all the crystals share the same deformation gradient, limiting the accuracy of the models. Under this constraint, heat conduction at the microscale is neglected and instantaneous temperature equilibrium is assumed. More recently, computational polycrystalline homogenization based on finite elements has been used to model the thermo-mechanical response of a polycrystal considering a detailed representation of the microstructure and resolving the microfields within the grains. Most of the studies [34, 35] use microscopic adiabatic conditions and therefore neglect thermal transport phenomena at the microscale, resulting in a very heterogeneous temperature distribution due to the differences in plastic dissipation in different points of the microstructure. In the last years, two fully coupled models for crystal plasticity have been presented that include heat diffusion at the microscale. In [36], a fully coupled thermodynamical framework using implicit integration is developed. The model includes heat generation and thermal strains but the crystal plastic behavior was assumed to be independent of the temperature. An alternative thermo-mechanical coupled framework was proposed recently for FCC materials [37] including a more physical description of the plastic flow in the crystal plasticity model, but formulated using an explicit time integration. It must be noted, finally, that none of the works reviewed proposing coupled thermo-mechanical frameworks for polycrystals considers the use of periodic boundary conditions for both thermal and mechanical fields, limiting the accuracy of the schemes proposed due to the inaccuracies near the RVE surfaces.

In this work we propose a fully coupled thermo-mechanical framework for computational homogenization of polycrystals to bridge the plastic deformation and temperature gradients at the macroscopic scale with the microscopic slip at the grain scale. This framework includes (1) Strong thermo-mechanical coupling, including thermal strains and temperature dependency of the crystal behavior through a physically based crystal plasticity model including temperature dependency of plastic slip and heat generation by dissipation due to plastic deformation. (2) Periodic boundary conditions in both the mechanical and thermal problems to account in the most accurate way with the polycrystalline homogenization problem or FE2 procedure. (3) An implicit implementation of the equations. (4) An experimental benchmark in a real polycrystal including several cases to assess the validity and accuracy of the model.

The thermo-mechanical homogenization problem is solved using Finite Element simulations in Representative Volume Elements of the microstructure

(RVEs) and periodic boundary conditions. During the deformation heat is generated at the grain scale due to plastic dissipation and then diffused throughout the body giving rise to thermal deformations and, thanks to the use of a temperature dependent CP formulation, modifying the mechanical response of the crystals. Both the crystal plasticity model and the heat conduction model are implemented in the commercial finite element code ABAQUS/Standard. In addition to the computation polycrystalline framework, the results of a homogenization model based on the Taylor approach are presented to show the effect of considering heat conduction at the microscale.

The remainder of this paper is organized as follows. In Section 2, a brief description of a general thermo-mechanical coupled problem is introduced, followed by a detailed introduction of the crystal plasticity model for single crystal and the computational homogenization approach that extracts the macroscopic material behavior from the finite element solution of a boundary value problem of a representative volume element. In Section 3, the numerical method for updating the deformation field and the temperature field is presented. In Section 4, a series of numerical examples are presented to validate the proposed framework. Finally, some concluding remarks are drawn.

## 2. Thermo-Mechanically Coupled Crystal Plasticity Modeling Framework

In this section, we start from the discussion of the general thermo-mechanical coupled analysis, and then we give a detailed introduction of the crystal plasticity constitutive model and the two homogenization approaches considered, the Taylor model and the full field computational homogenization approach.

### 2.1. Thermo-Mechanical Coupled Analysis

A thermo-mechanical problem is governed by the balance equations of linear momentum and energy. For quasi-static problems, the former can be written as

$$\nabla \cdot \boldsymbol{\sigma} + \mathbf{b} = \mathbf{0}, \quad (1)$$

where  $\boldsymbol{\sigma}$  is the Cauchy stress tensor,  $\mathbf{b}$  is the body force per unit of deformed volume, and  $\nabla \cdot$  is the spatial divergence operator. This equilibrium equation must hold for every  $\mathbf{x} = \boldsymbol{\varphi}(\mathbf{X}, t)$ , where  $\mathbf{X}$  denotes the coordinates of points of the body  $\mathcal{B}_0$  in the reference configuration,  $t$  refers to time, and  $\boldsymbol{\varphi}$  is the deformation mapping. The boundary  $\partial\mathcal{B}_0$  can be split in two disjoint parts denoted  $\partial_\varphi\mathcal{B}_0$  and  $\partial_t\mathcal{B}_0$ . Then, in addition to equilibrium condition (1) of points inside  $\mathcal{B}_0$ , the deformation must satisfy  $\boldsymbol{\varphi} = \bar{\boldsymbol{\varphi}}$  on  $\partial_\varphi\mathcal{B}_0$  and  $\boldsymbol{\sigma}\mathbf{n} = \mathbf{t}$  on  $\partial_t\mathcal{B}_0$ , where  $\mathbf{n}$  is the outer normal to the boundary and  $\mathbf{t}$  is a known field of surface tractions.

The second equation that describes the thermo-mechanical problem is the one imposing the balance of energy. If there are no external heat sources, and heat conduction follows Fourier's law, this equation reads

$$\rho c \dot{\theta} = \nabla \cdot (\mathbf{k} \nabla \theta) + \dot{Q}_V. \quad (2)$$

Here  $\theta$  denotes the absolute temperature,  $\rho$  refers to the mass per unit of deformed volume,  $c$  is the specific heat capacity,  $\mathbf{k}$  is the spatial conductivity tensor, and  $\dot{Q}_V$  is the internal heat generation rate per unit of deformed volume. Eq. (2) must be satisfied in every point of the interior  $\mathcal{B}_0$ . As in the case of the mechanical problem, the boundary of the body can be split into two disjoint sets  $\partial_h \mathcal{B}_0$  and  $\partial_\theta \mathcal{B}_0$ . The thermal problem is completed with Dirichlet boundary conditions for the temperature on  $\partial_\theta \mathcal{B}_0$  and Neumann conditions for the heat flux on  $\partial_h \mathcal{B}_0$ .

The evaluation of the stress tensor  $\boldsymbol{\sigma}$ , as a function of the current and past values of the deformation and temperature, is the central problem of solid thermo-mechanics. In continuum thermo-mechanics with internal variables, it is assumed that the stress tensor depends on the deformation gradient  $\mathbf{F} = \nabla_0 \boldsymbol{\varphi}$ , its rate  $\dot{\mathbf{F}}$ , the local value of  $\theta$  and, possibly, some internal variables denoted collectively as  $\boldsymbol{\xi}$ . That is,

$$\boldsymbol{\sigma} = \hat{\boldsymbol{\sigma}}(\mathbf{F}, \dot{\mathbf{F}}, \theta, \boldsymbol{\xi}). \quad (3)$$

In the definition of  $\mathbf{F}$  and below,  $\nabla_0$  refers to the material gradient operator.

The constitutive law described by Eq. (3) strongly couples Eqs. (1) and (2), and hence the deformation and temperature fields. As will be shown later when a specific form of this constitutive relation is provided, temperature changes induce thermal strains and changes in the mechanical constants; in turn, the dissipation due to the power of the stress conjugated with the viscoplastic strains generates internal heat  $\dot{Q}_V$ . efficiency of the conversion of mechanical into thermal energy is not perfect because some energy is stored in microstructural transformations at the dislocation level. However, considering this phenomena from a physical view point implies the introduction of constitutive hypotheses that are material dependent (see, e.g., the discrete dislocation model presented by Benzerga et. al. for copper [38]). A general framework should rely on the experimental measure of the fraction of energy transformed in heat through a coefficient that might vary from case to case. This type of approach was proposed by Taylor and Quinney by introducing a coefficient expressing the efficiency of this transformation. This is the approach taken here, more specifically, the internal heat generation is customarily expressed as

$$\dot{Q}_V = \chi \dot{W}^p \quad (4)$$

where  $\dot{W}^p$  is the plastic power and  $\chi$  is the so-called Taylor-Quinney parameter, usually selected in the range  $0.85 \leq \chi \leq 1.0$ .

As a result of the previous arguments, we conclude that an accurate solution of both the mechanical and thermal problems is required in order to solve the fully coupled problem. Moreover, the constitutive relation is identified as the critical and more complex part of the solution, and responsible for the coupling. Based on this reasoning, and in order to get the most reliable possible model for metallic materials, a general crystal plasticity model is chosen in which plastic flow is aided by thermal activation. This type of temperature dependency of

the plastic behavior can be found in BCC metals, in HCP deforming under pyramidal slip or in FCC alloys hardened by precipitates.

## 2.2. Crystal Plasticity Model for a Single Crystal

For finite strain inelastic mechanics of single crystal plasticity the deformation gradient  $\mathbf{F}$  is assumed to be multiplicatively decomposed in its elastic and plastic parts as in  $\mathbf{F} = \mathbf{F}^e \mathbf{F}^p$  [39]. The elastic and plastic deformation gradients define two different *local* deformed configurations: one *intermediate* configuration described by  $\mathbf{F}^p$ , and the final deformed configuration locally determined by  $\mathbf{F}^e \mathbf{F}^p$ . For a thermo-mechanical problem, a third configuration is introduced accounting for thermal deformations [40]. The resulting decomposition reads

$$\mathbf{F} = \mathbf{F}^e \mathbf{F}^p \mathbf{F}^\theta, \quad \det \mathbf{F}^e > 0, \quad \det \mathbf{F}^p = 1, \quad \det \mathbf{F}^\theta > 0. \quad (5)$$

where  $\mathbf{F}^\theta$  now represents the thermal part of the deformation gradient. The elastic deformation gradient embodies the elastic distortions of the lattice, and the rigid body motions; the plastic part,  $\mathbf{F}^p$ , describes the irreversible deformations of the lattice, associated with plastic shearing along crystallographic planes; finally, the thermal contribution  $\mathbf{F}^\theta$  includes the lattice distortion due solely to thermal effects. The local configuration defined by  $\mathbf{F}^p \mathbf{F}^\theta$  is hereafter called the intermediate configuration, and can be regarded as being obtained by a pure elastic unloading from the current configuration.

The constitutive model relates the three parts of the deformation gradient with the stress and temperature, or their evolution. In particular, the evolution of the thermal deformation gradient of any metal can be expressed respect its lattice symmetry axis as

$$\dot{\mathbf{F}}^\theta \mathbf{F}^{\theta^{-1}} = \dot{\theta} \boldsymbol{\beta}, \quad (6)$$

where  $\boldsymbol{\beta}$  is a diagonal tensor of anisotropic thermal expansion coefficients

$$\boldsymbol{\beta} = \text{diag}(\beta_1, \beta_2, \beta_3). \quad (7)$$

Assuming that the plastic deformation takes place purely through dislocation glide, the evolution of the plastic deformation gradient could be expressed as a combination of the slip rate  $\dot{\gamma}^\alpha$  in every slip system  $\alpha$  as in

$$\dot{\mathbf{F}}^p \mathbf{F}^{p^{-1}} = \sum_{\alpha} \dot{\gamma}^\alpha \mathbf{S}_0^\alpha, \quad (8)$$

where, for every slip system  $\alpha$ ,  $\mathbf{S}_0^\alpha = \mathbf{s}_0^\alpha \otimes \mathbf{m}_0^\alpha$  is the Schmidt tensor,  $\mathbf{s}_0^\alpha$  and  $\mathbf{m}_0^\alpha$  are unit vectors along the slip direction and normal to the slip plane, respectively.

In the intermediate configuration, the elastic Green-Lagrange strain  $\mathbf{E}^e$  is defined as

$$\mathbf{E}^e = \frac{1}{2} \left( \mathbf{F}^{eT} \mathbf{F}^e - \mathbf{I} \right), \quad (9)$$

where  $\mathbf{I}$  is the second order identity tensor. Let  $\mathbf{S}^*$  be second Piola-Kirchhoff tensor, the stress that is work conjugate to  $\mathbf{E}^e$ . An elastic constitutive relation is given by

$$\mathbf{S}^* = \mathcal{L} : \mathbf{E}^e, \quad (10)$$

where  $\mathcal{L}$  is the fourth-order temperature dependent elasticity tensor.

The Cauchy stress is the push forward of the stress  $\mathbf{S}^*$  to the current configuration, that is

$$\boldsymbol{\sigma} = (\det \mathbf{F}^e)^{-1} \mathbf{F}^e \mathbf{S}^* \mathbf{F}^{eT}. \quad (11)$$

To close the mechanical constitutive law, the evolution of the plastic slip  $\gamma^\alpha$  must be specified for every slip plane. In a viscoplastic model, the slip rate is expressed with the flow model

$$\dot{\gamma}^\alpha = \hat{\gamma}^\alpha(\tau^\alpha, s^\alpha, \theta), \quad (12)$$

where  $\tau^\alpha$  is the resolved shear stress in slip system  $\alpha$ , defined as

$$\tau^\alpha = \det \mathbf{F}^\theta \left( \mathbf{F}^{\theta T} \mathbf{S}^* \mathbf{F}^{\theta -T} \right) \cdot \mathbf{S}_0^\alpha, \quad (13)$$

and  $s^\alpha$  is the slip resistance [40]. In this equation, and below, the dot product refers to the full contraction of vectors or tensors over all their indices. The quantity  $s^\alpha$  evolves following the hardening model

$$\dot{s}^\alpha = \sum_{\beta} h^{\alpha\beta} |\dot{\gamma}^{\beta}|, \quad (14)$$

where

$$h^{\alpha\beta} = h^\alpha q^{\alpha\beta} \quad (15)$$

represents the hardening modulus,  $q^{\alpha\beta}$  stands for the latent hardening coefficients, and  $h^\alpha$  is the self hardening modulus.

Several flow and hardening models have been proposed in the literature [41, 42, 43, 44]. In this work, a physically based flow model including temperature dependency is combined with a phenomenological hardening model in order to provide a relatively general CP framework that can be adapted in principle to many different alloys [30, 32].

Assume that the slip resistance  $s^\alpha$  could be decomposed as

$$s^\alpha = s_{at}^\alpha + s_t^\alpha, \quad (16)$$

where  $s_t$  and  $s_{at}$  denote the thermal and athermal parts due to thermally activated obstacles and athermal obstacles, respectively [32]. The resolved shear stress at slip system  $\alpha$  needs to overcome the athermal part of the slip resistance before slip starts. Beyond that value of the resolved shear stress, the thermal energy required to overcome the obstacle depends on the effective resolved shear stress  $\tau_{eff}^\alpha$ , defined as

$$\tau_{eff}^\alpha = |\tau^\alpha| - s_{at}^\alpha. \quad (17)$$

According to the flow model proposed by Frost and Ashby[42], the slip rate in a slip system  $\alpha$  controlled by some thermal activation process can be obtained from the Orowan equation

$$\dot{\gamma}^\alpha = \rho_m^\alpha b^\alpha \bar{L} \bar{\nu}^\alpha(\tau_{eff}^\alpha, \theta). \quad (18)$$

where  $\rho_m^\alpha$  denotes the mobile dislocation density,  $b^\alpha$  the Burgers vector of that system and  $\bar{L}$  is a characteristic length of the distance between obstacles.  $\bar{\nu}^\alpha$  is the average frequency of jumping events across the obstacles, depends both on the effective resolved stress and the current temperature and is obtained using the theory of thermally activated processes. If all the constants in the previous equation are grouped, a single parameter independent of the temperature  $\dot{\gamma}_0^\alpha$ , the reference slip rate, can be defined as

$$\dot{\gamma}_0^\alpha \approx \rho_m^\alpha b^\alpha \bar{L} \nu_0, \quad (19)$$

where  $\nu_0$  is the Debye frequency. Using this value, the shear rate can finally be expressed as

$$\dot{\gamma}^\alpha = \begin{cases} 0, & \tau_{eff}^\alpha \leq 0, \\ \dot{\gamma}_0^\alpha \exp\left(-\frac{\Delta G^\alpha}{k_B \theta}\right) \text{sign}(\tau^\alpha), & 0 < \tau_{eff}^\alpha \leq s_t^\alpha, \end{cases} \quad (20)$$

where  $k_B$  is Boltzmann's constant and  $\Delta G^\alpha$  is the activation enthalpy. The latter can be obtained with the expression

$$\Delta G^\alpha = \Delta F^\alpha \left[ 1 - \left( \frac{|\tau_{eff}^\alpha|}{s_t^\alpha} \right)^p \right]^q, \quad (21)$$

with  $\Delta F^\alpha$  being the activation energy at 0 K,  $p$  and  $q$  denoting model parameters with values  $0 < p < 1$  and  $1 < q < 2$ .

The flow model based on thermal activation is valid for any alloy in which dislocation glide is controlled by thermal activation. In BCC crystals, the lattice friction is the main energy barrier and it is usually assumed that the thermal part of the slip resistance  $s_t^\alpha$  is constant [32]. For FCC crystals, the short range dislocation-dislocation interactions are the main thermal process and it was investigated experimentally [45] that both the thermal and athermal parts of the slip resistance evolve with the deformation but their ratio  $s_t^\alpha/s_{at}^\alpha$  could be regarded as a constant over a broad range of strains. In this study  $s_t^\alpha$  is considered independent of the accumulated plastic slip (BCC case), and the self hardening modulus  $h^\alpha$  in Eq. (15) for describing the evolution of the slip resistance is given by a phenomenological hardening model as

$$h^\alpha = h_0^\alpha (1 - s_{at}^\alpha/s_s^\alpha)^{r_1} \text{sign}(1 - s_{at}^\alpha/s_s^\alpha). \quad (22)$$

where  $h_0^\alpha$  is the initial hardening moduli,  $r_1$  is a model parameter, and  $s_s^\alpha$  is the saturation value of  $s_{at}^\alpha$ .



Finally, the volumetric heat generation contributed from plastic work dissipation defined in Eq. (4) can be evaluated to be

$$\dot{Q}_V = \chi \sum_{\alpha} \tau_{\alpha} \dot{\gamma}_{\alpha}. \quad (23)$$

### 2.3. Polycrystal computational homogenization

For metallic materials, every macroscopic material point is associated with a collection of single crystals characterized by their shapes and orientations, and the behavior of a material point is determined by the collective responses of the single crystals or grains. The relation between the macroscopic or polycrystalline response and the crystal behavior depends on the actual microstructure (grain shape and orientation distributions) and is given by the theory of homogenization. The simplest approach is the so-called Taylor model [46], which assumes that the local deformation gradient in each grain is constant and identical to the deformation gradient of the macroscopic material point. In this case each grain is considered to be an independent single crystal with prescribed initial volume and orientation, while interactions between neighboring grains are neglected. The macroscopic response of the material point is extracted simply by averaging the responses of all the associated grains. More refined homogenization models also consider a constant value of the fields in each grain (mean-field models) but allow that each grain deforms independently based on its actual orientation. The viscoplastic self-consistent model (VPSC) is the most common approach within mean-field approaches [47, 48, 49] and due to its accuracy and relative simplicity can be used as constitutive equation of a polycrystal in macroscopic simulations [50]. However, meanfield approaches are not accurate enough for some purposes and computational homogenization schemes are preferred.

The computational homogenization of polycrystals is based on the numerical resolution, usually with the Finite Element method, of the governing equations at the microscopic level in a representative volume element (RVE) of the polycrystalline microstructure [51, 8]. The RVE typically contains hundreds of grains, each one with an assigned initial orientation and represented by a subset of material points so that the orientation distribution function (ODF) and the distribution of the grain size in the RVE reproduce, in a statistical sense, the corresponding distribution functions experimentally measured. The macroscopic fields are obtained as the volume average of the microscopic fields obtained by the numerical resolution of a boundary value problem in the RVE. Compared to mean-field approaches, computational homogenization accounts for a more detailed description of the microstructure evolution and the full resolution of the fields at the micro-scale result in a more accurate prediction of the macroscopic behavior of the material.

Computational homogenization is the basis of the model proposed in this work to describe the thermo-mechanical response of a polycrystal. Nevertheless, a simpler homogenization model based on Taylor’s approach is also considered in order to show the effect in the mechanical response of considering heat dif-

fusion at the microscale. The main equations describing both homogenization approaches are given next.

*Taylor model*

The Taylor model is a mean-field approach and assumes that the deformation gradient in each grain is represented by its mean value and is identical to the macroscopic deformation gradient,  $\bar{\mathbf{F}}$ . In the thermo-mechanical case, the temperature in each grain is also represented by its mean value  $\theta^{(k)}$  and it is considered that each grain only contributes to its local temperature rise, assuming an adiabatic condition at the microscale. Under these approaches, micro- and macro- fields are related as

$$\begin{aligned}\bar{\mathbf{F}} &= \mathbf{F}^{(k)} \\ \bar{\boldsymbol{\sigma}} &= \frac{1}{N_c} \sum_{k=1}^{N_c} \boldsymbol{\sigma}^{(k)} \\ \bar{\theta} &= \frac{1}{N_c} \sum_{k=1}^{N_c} \theta^{(k)}\end{aligned}\tag{24}$$

where  $N_c$  is the total number of grains/orientations considered to represent the polycrystal,  $\bar{\mathbf{F}}$ ,  $\bar{\boldsymbol{\sigma}}$  and  $\bar{\theta}$  stand, respectively, for the macroscopic values of the deformation gradient, stress and temperature and  $k$  labels a grain.

*Computational homogenization framework*

Our computational homogenization framework is based on solving numerically the governing Eqs. (1) and (2) with periodic boundary conditions using the Finite Element method. The stress tensor and the temperature of a macroscopic material point are calculated, respectively, with the averages:

$$\begin{aligned}\bar{\boldsymbol{\sigma}} &= \frac{1}{V} \int \boldsymbol{\sigma} \, dV = \frac{1}{N} \sum_{k=1}^N \boldsymbol{\sigma}^{(k)} W^{(k)} \\ \bar{\theta} &= \frac{1}{V} \int \theta \, dV = \frac{1}{N} \sum_{k=1}^N \theta^{(k)} W^{(k)},\end{aligned}\tag{25}$$

where  $N$  is the total number of integration points within the RVE and  $W^{(k)}$  is the volume element associated to the  $k$ -th quadrature point.

The microstructure of a polycrystalline material can be idealized as an infinite periodic arrangement of a RVEs. Under this approach, periodic boundary conditions need to be imposed to enforce shape compatibility between adjacent deformed RVEs. Periodic boundary conditions reproduce exactly the deformation of an infinite media constructed by a periodic arrangement of the RVE. Moreover, it has been observed that, among the different boundary conditions that fulfill the Hill-Mandel condition, periodic boundary conditions give solutions that converge faster than any other to the solution of an infinite RVE

[52]. For a cubic RVE, let  $P_i^+$  be an arbitrary node lying on a boundary surface  $S_i^+$ , and  $P_i^-$  be its counterpart lying on surface  $S_i^-$ , where  $S_i^+$  and  $S_i^-$  are a pair of surfaces perpendicular to the  $X_i$  axis. According to the requirement of periodicity and continuity of boundary conditions, the deformations of nodes  $P_i^+$  and  $P_i^-$  are linked by the multiple point constraints given by [53],

$$\mathbf{u}(P_i^+) - \mathbf{u}(P_i^-) = (\bar{\mathbf{F}} - \mathbf{I})\mathbf{L}_i = \mathbf{u}(M_i) - \mathbf{u}(O) \quad (i = 1, 2, 3), \quad (26)$$

where  $\bar{\mathbf{F}}$  is the deformation gradient of the corresponding macroscopic material point,  $\mathbf{L}_i$  is a vector with the length of the cubic RVE along the  $X_i$  axis and  $O$  and  $M_i$  being its two associated vertices. The vertex  $O$  is called the reference point and its deformation  $\mathbf{u}(O)$  is set to zero for convenience.

In the case of the thermal problem, the use of periodic boundary conditions on temperature in the RVE also provides the microscopic temperature distribution in an idealized medium formed as an infinite periodic arrangement of the RVE. In this case, the corresponding equations are

$$\theta(P_i^+) - \theta(P_i^-) = \nabla\bar{\theta}_i \cdot \mathbf{L}_i = \theta(M_i) - \theta(O) \quad (i = 1, 2, 3), \quad (27)$$

where  $\nabla\bar{\theta}$  is the temperature gradient of the macroscopic material point and  $\mathbf{L}_i, M_i, O$  are as before.

From the macroscopic view point, two cases of interest can be analyzed with the periodic RVE, namely, adiabatic and isothermal processes. In the case of an adiabatic process the average temperature gradient  $\nabla\bar{\theta}$  is equal to zero. In this case, Eq. (27) is reduced to

$$\theta(P_i^+) - \theta(P_i^-) = 0 \quad (i = 1, 2, 3). \quad (28)$$

In standard constitutive models at the macroscale, the adiabatic condition assumes that the plastic work contributes to the macroscopic temperature increase locally and that its effect on the mechanical response is instantaneous. On the contrary when two scales are considered, the heat generation at the micro-scale is not uniform due to the inhomogeneous distributions of the stress, plastic strain and temperature fields caused by the heterogeneity of the microstructure. In this case thermal conduction exists between grains at the microscopic level even under macroscopic adiabatic conditions and the mechanical effect of the temperature at the macro-scale might not be instantaneous. Such a detailed description of the distribution and evolution of the temperature field within the RVE is obtained in this work by solving a thermo-mechanically coupled problem under the periodic boundary conditions given in Eqs. (26) and (28). The additional complexity of the coupled problem leads to a better prediction of the material behavior during thermo-mechanical processes, as compared to the conventional approaches.

The second case of interest is a macroscopic isothermal process. In this case, to ensure that the temperature of the macroscopic material point does not change in time, the average temperature increase of the associated RVE should be kept equal to zero at all times. This could be implemented simply by setting equal to zero the Taylor-Quinney factor  $\chi$  defined in Eq. (4).

### 3. Numerical Methods

#### 3.1. Taylor model

Under Taylor's homogenization model, the macroscopic deformation is prescribed and it is assumed that its value is equal to the deformation gradient of each crystal. Hence, there is no need to solve any boundary value problem at the microscale. The problem is reduced to solve, for each time increment, the system of non-linear equations defined by the constitutive equations, summarized in section 2.2, and the Taylor approach given by Eq. (24).

To obtain the macroscopic stress and temperature as functions of the current deformation gradient, the backward Euler method is used to integrate the equations in time. The time interval of interest is divided into subintervals of size  $\Delta t$ . Let  $\bar{\mathbf{F}}_{n+1}$  be the prescribed macroscopic deformation gradient at time  $t = t_{n+1}$  and  $\boldsymbol{\sigma}^{(k)}$  the stress in the  $k$ -th grain of the polycrystal. The problem to solve consists in finding for each grain  $k$  its stress  $\boldsymbol{\sigma}^{(k)}$ , temperature,  $\theta^{(k)}$  and internal variables  $\boldsymbol{\xi}^{(k)}$  that satisfy the constitutive equation (3) at time  $t_{n+1}$ , that is,

$$\boldsymbol{\sigma}^{(k)} = \hat{\boldsymbol{\sigma}} \left( \mathbf{F}^{(k)}, \dot{\mathbf{F}}^{(k)}, \theta^{(k)}, \boldsymbol{\xi}^{(k)} \right) = \hat{\boldsymbol{\sigma}} \left( \bar{\mathbf{F}}_{n+1}, \dot{\bar{\mathbf{F}}}_{n+1}, \theta^{(k)}, \boldsymbol{\xi}^{(k)} \right). \quad (29)$$

The numerical scheme for updating the local stress of each grain in Eq. (29) is discussed in detail in Section 3.2.2.

The temperature at each grain,  $\theta^{(k)}$  in Eq. (29) is computed from the local temperature at time  $t_n$  and its increment from  $t_n$  to  $t_{n+1}$ , denoted as  $\Delta\theta^{(k)}$ , using the thermal balance equation and neglecting heat conduction between grains

$$\Delta\theta^{(k)} = \dot{Q}_V^{(k)}(\boldsymbol{\sigma}^{(k)}, \boldsymbol{\xi}^{(k)}). \quad (30)$$

A fixed-point iteration algorithm is used to solve, for each grain, the system of non-linear equations (29) and (30). The values of  $\theta^{(k)}$  and  $\boldsymbol{\xi}^{(k)}$  are initialized at the beginning of the time step with the corresponding values at the previous time and are updated iteratively. This iterative procedure is repeated until the differences of the stress and temperature between two consecutive iterations are below a given tolerances.

Once the non-linear equations are solved, the macroscopic stress  $\bar{\boldsymbol{\sigma}}$  and the temperature  $\bar{\theta}$  at the material point are computed as the average of the values in each grain as

$$\begin{aligned} \bar{\boldsymbol{\sigma}} &= \frac{1}{N_c} \sum_{k=1}^{N_c} \boldsymbol{\sigma}^{(k)} \\ \bar{\theta} &= \frac{1}{N_c} \sum_{k=1}^{N_c} \theta^{(k)} \end{aligned} \quad (31)$$

### 3.2. Computational homogenization approach

#### 3.2.1. Iterative solution scheme for the coupled fields

The governing equations of the coupled problem, namely Eqs. (1) and (2), need to be satisfied simultaneously at any time. For this combination of nonlinear equations, a nonlinear incremental method is employed. In each increment, a two-level iterative scheme is applied to solve the equations in a staggered way. First, the deformation  $\boldsymbol{\varphi}$  is found by solving the equilibrium equation (1) at a fixed temperature field. Then, the temperature  $\theta$  is obtained as the solution of the balance of energy equation at the newly updated deformation. The procedure is repeated until both balance equations are solved below a given tolerance.

To solve for the deformation and temperature, a finite element discretization is employed in space, and a backward Euler method is used to integrate the equations in time. For the spatial discretization, we consider a partition of the body into a finite number of hexahedra, defining a finite element space of shape functions  $N_a : \mathcal{B} \rightarrow \mathbb{R}$ , where  $a = 1, \dots, n_{node}$ , and  $n_{node}$  is the number of nodes in the mesh. As in the case of the Taylor approach we partition the time interval of interest into subintervals of size  $\Delta t$ , and indicate with the subscript  $(\cdot)_n$  the value of any function at time  $t_n = n \Delta t$ . Using the shape functions, the finite element approximation of the deformation and temperature fields at time  $t_n$ , denoted respectively as  $\boldsymbol{\varphi}_n^h$  and  $\theta_n^h$ , can be expressed as

$$\boldsymbol{\varphi}_n^h(\mathbf{X}) = \sum_{a=1}^{n_{node}} N_a(\mathbf{X}) \boldsymbol{\varphi}_n^a, \quad \theta_n^h(\mathbf{X}) = \sum_{a=1}^{n_{node}} N_a(\mathbf{X}) \theta_n^a. \quad (32)$$

The quantities  $\boldsymbol{\varphi}_n^a, \theta_n^a$  denote the *nodal* values of the deformation and temperature, respectively, at time  $t_n$ .

The Galerkin form of the equilibrium equation (1) is obtained as follows. Given any admissible deformation variation  $\delta\boldsymbol{\varphi}^h$ , the weak form of the balance of linear momentum can be written as

$$0 = \int_{\mathcal{B}} \boldsymbol{\sigma} \cdot \nabla \delta\boldsymbol{\varphi}^h \, dV - \int_{\partial\mathcal{B}} \mathbf{t} \cdot \delta\boldsymbol{\varphi}^h \, dS - \int_{\mathcal{B}} \mathbf{b} \cdot \delta\boldsymbol{\varphi}^h \, dV, \quad (33)$$

where  $\boldsymbol{\sigma}$  is the value of the Cauchy stress obtained at the solution of the plasticity model of Sections 2.2 and 2.3, evaluated at time  $t_{n+1}$  as detailed in Section 3.2.2.

Similarly, for a test temperature field  $\delta\theta^h$ , the backward Euler discretization of the weak form of Eq. (2) reads

$$\int_{\mathcal{B}} \left[ \rho c \frac{\theta_{n+1}^h - \theta_n^h}{\Delta t} \delta\theta^h + \nabla \theta_{n+1}^h \cdot \mathbf{k} \nabla \delta\theta^h - \dot{Q}_V \delta\theta^h \right] dV = 0. \quad (34)$$

As indicated previously, we have implemented the solution of Eqs. (33)-(34) in a staggered fashion: first, Eq. (33) is solved for  $\boldsymbol{\varphi}_{n+1}^h$ , for a fixed temperature; then, Eq. (34) is used to find the updated temperature  $\theta_{n+1}^h$ , for the previously obtained deformation. The two steps are repeated until both discrete balance equations are verified up to a given tolerance.

### 3.2.2. Update of Cauchy stress

The update of the stress tensor is the key part of the iterative process required to solve the nonlinear system of coupled equations. During each iteration, the thermal deformation gradient can be calculated directly from Eq. (6) as

$$\mathbf{F}_{n+1}^\theta = \exp(\Delta\theta\boldsymbol{\beta}) \mathbf{F}_n^\theta \approx (\mathbf{I} + \Delta\theta\boldsymbol{\beta}) \mathbf{F}_n^\theta, \quad (35)$$

with  $\Delta\theta = \theta_{n+1} - \theta_n$ . Next, using Eq. (5), the plastic deformation gradient can be evaluated with the expression

$$\mathbf{F}_{n+1}^p = \exp\left(\Delta t \sum_{\alpha} \dot{\gamma}^{\alpha} \mathbf{S}_0^{\alpha}\right) \mathbf{F}_n^p \approx \left(\mathbf{I} + \Delta t \sum_{\alpha} \dot{\gamma}^{\alpha} \mathbf{S}_0^{\alpha}\right) \mathbf{F}_n^p. \quad (36)$$

Replacing Eqs. (35) and (36) in Eq. (5), the elastic deformation gradient can be also obtained as

$$\mathbf{F}_{n+1}^e = \mathbf{F}_{n+1} \mathbf{F}_{n+1}^{\theta}{}^{-1} \mathbf{F}_n^{p-1} \left(\mathbf{I} - \Delta t \sum_{\alpha} \dot{\gamma}^{\alpha} \mathbf{S}_0^{\alpha}\right). \quad (37)$$

This expression can be rewritten as

$$\mathbf{F}_{n+1}^e - \mathbf{F}_{n+1} \mathbf{F}_{n+1}^{\theta}{}^{-1} \mathbf{F}_n^{p-1} \left(\mathbf{I} - \Delta t \sum_{\alpha} \dot{\gamma}^{\alpha} \mathbf{S}_0^{\alpha}\right) = 0. \quad (38)$$

Using an Euler backward scheme, the increment of the accumulated shear strain is given by

$$\Delta\gamma^{\alpha} = \dot{\gamma}^{\alpha} \Delta t. \quad (39)$$

Combining Eqs. (38) and (39), a set of nonlinear equations is formed, and the elastic deformation gradient  $\mathbf{F}_{n+1}^e$  and the increment of the accumulated shear strain  $\Delta\gamma^{\alpha}$  can be solved simultaneously, at the level of the quadrature point, with Newton-Raphson's method. Once the elastic deformation gradient of the current increment is obtained, the Cauchy stress is updated with Eqs. (9)-(11).

## 4. Numerical Examples

The computational framework proposed is applied to study the thermo-mechanical response of pure BCC tantalum under uniaxial traction. The results obtained with this numerical framework will be compared at the end of this section with the response obtained using the Taylor homogenization approach.

A RVE with 400 randomly oriented grains is defined and discretized in hexahedral finite elements, as illustrated in Fig. 1. To determine the size of the models a mesh sensitivity study was done to. In particular, simulations considering the macroscopic adiabatic condition were conducted using meshes containing  $20^3$ ,  $25^3$  and  $30^3$  elements to check the effects of mesh. It was observed that the difference of both the macroscopic temperature-strain curves and the stress-strain curves between the model with  $20^3$  mesh and  $30^3$  mesh were below 1%.

In addition, microscopic fields were also very similar. These results suggested that the mesh containing  $20^3$  elements is accurate enough, and this size is then used for the following part of the paper (Fig. 1). With respect to the number of crystals, it has been observed that 400 is a number sufficiently large to provide statistically representative results and isotropic response.

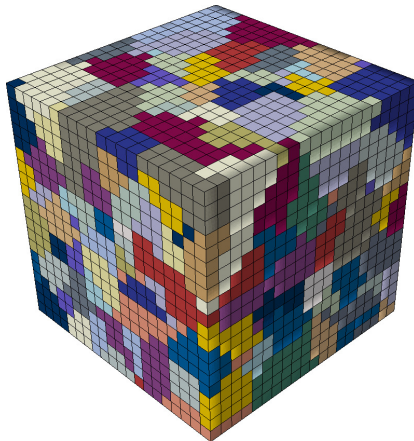


Figure 1: Representative volume element of BCC Ta containing 400 randomly-oriented crystals discretized with 8000 cubic finite elements.

The elastic moduli (in GPa) of this metallic material is approximated by a linear function of the temperature  $\theta$  as follows [54]:

$$\begin{aligned} c_{11} &= 268.2 - 0.024 \theta, \\ c_{12} &= 159.6 - 0.011 \theta, \\ c_{44} &= 87.1 - 0.015 \theta. \end{aligned} \tag{40}$$

The density, the specific heat, the thermal conductivity and the thermal expansion are taken to be  $16.69 \times 10^3 \text{ Kg/m}^3$ ,  $1.506 \times 10^8 \text{ J/(Kg} \cdot \text{K)}$ ,  $57.5 \text{ W/(m} \cdot \text{K)}$  and  $6.3 \times 10^{-6} \text{ K}^{-1}$ , respectively.

Regarding the plastic response, in BCC metals three sets of slip systems are normally responsible of the plastic deformation,  $\langle 111 \rangle \{110\}$ ,  $\langle 111 \rangle \{112\}$  and  $\langle 111 \rangle \{123\}$ . In this work, only the first two slip sets are taken into consideration as proposed in [32] and the corresponding slip systems are listed in Table 1. The experimental behavior of Tantalum was taken from [55] where an enhanced compression recovery split Hopkinson bar technique was used to obtain the plastic flow in wide range of strains, strain rates, and temperatures during uniaxial compression. In particular, the model parameters defining both flow and hardening model were adjusted to fit the stress-strain response of the polycrystalline RVE with the experimental result for the case of uniaxial traction under isothermal condition in [55]. This fitting procedure used in the study started using the set of parameters for the flow and hardening model in [32] as an initial guess. It must be noted that the resulting parameters are different to

Table 1: Slip Systems for BCC Ta

$\alpha$	$s_0$	$m_0$	$\alpha$	$s_0$	$m_0$
1	1 1 $\bar{1}$	0 1 1	13	$\bar{1}$ 1 1	2 1 1
2	1 $\bar{1}$ 1	0 1 1	14	1 1 1	$\bar{2}$ 1 1
3	$\bar{1}$ 1 1	0 1 $\bar{1}$	15	1 1 $\bar{1}$	2 $\bar{1}$ 1
4	1 1 1	0 1 $\bar{1}$	16	1 $\bar{1}$ 1	2 1 $\bar{1}$
5	1 1 $\bar{1}$	1 0 1	17	1 $\bar{1}$ 1	1 2 1
6	$\bar{1}$ 1 1	1 0 1	18	1 1 $\bar{1}$	$\bar{1}$ 2 1
7	1 $\bar{1}$ 1	1 0 $\bar{1}$	19	1 1 1	1 2 1
8	1 1 1	1 0 $\bar{1}$	20	$\bar{1}$ 1 1	1 2 $\bar{1}$
9	$\bar{1}$ 1 1	1 1 0	21	1 1 $\bar{1}$	1 1 2
10	1 $\bar{1}$ 1	1 1 0	22	1 $\bar{1}$ 1	$\bar{1}$ 1 2
11	1 1 $\bar{1}$	1 $\bar{1}$ 0	23	$\bar{1}$ 1 1	1 $\bar{1}$ 2
12	1 1 1	1 $\bar{1}$ 0	24	1 1 1	1 1 2

the ones obtained in [32] because their polycrystalline framework was based on Taylor's model, which gives an upper bound for the stress predictions, while the present approach is based on computational homogenization. The resulting set of parameters obtained are listed in Table 2.

Table 2: Material Properties of BCC Ta

Model Parameter	Value
$\Delta F^\alpha$	$2.77 \cdot 10^{-19}$ J
$\dot{\gamma}_0$	$1.732 \cdot 10^7$ s $^{-1}$
$h_0$	181 MPa
$s_s$	121 MPa
$r_1$	1.10
$p$	0.28
$q$	1.40
$s_{at,0}$	50.0 MPa
$s_{t,0}$	445 MPa

To assess the validity of the fitting procedure, the parameters listed in Table 2 (fitted using isothermal experiments) are used in the numerical framework to predict the stress-strain response of the RVE under an adiabatic condition. The numerical results and corresponding experimental results obtained from [55] are plotted in Fig. 2. It is shown that the numerical predictions provided by the current work are in good agreement with the experimental results, which validates the reliability of this proposed framework.

#### 4.1. Effects of initial orientation

To study the effect of the initial orientation on the responses of single crystal Ta, a single crystal RVE is created and discretized into  $20 \times 20 \times 20$  regular finite elements, as in the first simulation. The solid is strained at three different crystalline directions [1 0 0], [1 1 0] and [1 1 1]. The uniaxial stress-strain curves



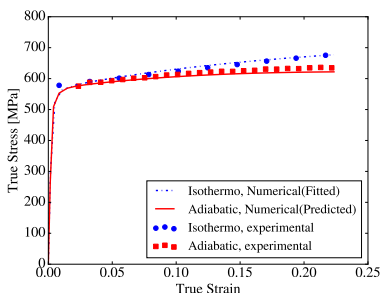


Figure 2: Comparison of experimental and predicted stress-strain responses of BCC Ta during uniaxial traction.

and the temperature changes at these directions during traction processes under adiabatic condition are plotted in Fig. 3.

It is shown that the response of the single crystal is closely dependent on the traction direction, being the strength obtained when loading in direction  $[1\ 1\ 1]$  the highest of all the three cases. In the model, the same value of  $s_{at}$  and  $s_t$  are chosen for all the slip systems so the result obtained is simply due to the Schmidt factor of the systems. In particular, when loading in a  $[1\ 1\ 1]$  direction the Schmidt factor of the best oriented planes is lower than in the other two loading directions and therefore, the material plastifies at a larger applied stress.

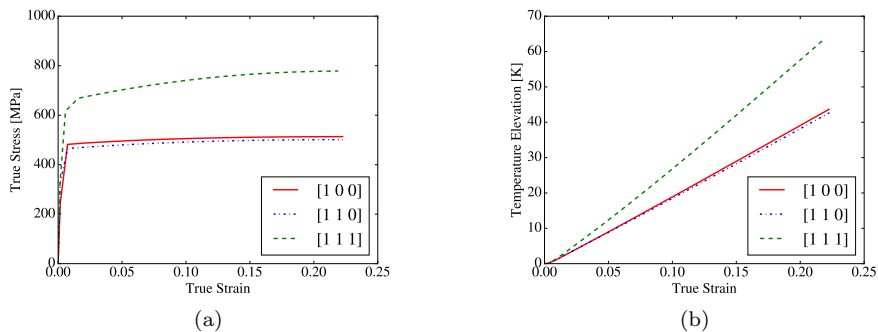


Figure 3: (a). Uniaxial stress-strain and (b). Temperature change-strain curves of single crystalline BCC Ta during uniaxial traction at various crystallographic directions

The implications of the loading direction of the single crystal in the thermal response can be observed in Fig. 3. The temperature rises faster when loading in the  $[111]$  direction and this is due to the higher strength in this direction. Heat generation is proportional to the plastic dissipation which rate depends on the sum of the product of resolved stress and shear rates on all the systems (Eq. (23)). Because the accumulated plastic shear is the same for all the three loading directions, the temperature increases faster when pulling in the  $[111]$

direction due to its larger strength.

#### 4.2. Effects of initial temperature

To study the effect of the initial temperature on the thermo-mechanical behavior of polycrystalline Ta, the RVE is strained at three different initial temperatures: 298 K, 398 K, and 498 K with an engineering strain rate of  $5000 \text{ s}^{-1}$ . Two sets of simulations are performed, under isothermal conditions and under adiabatic conditions in order to quantify the effect of considering heat generation during the test. The numerical results of the mechanical response of both type of tests are plotted in Fig. 4(a). It can be observed that the effect of the initial temperature is a decrease in the material strength. In the isothermal case, all the three curves are proportional and hardening is not affected by the initial temperature. Under adiabatic conditions, the material plastifies at the same stress than as in the corresponding isothermal case but the stress-strain curve deviates with the strain showing less hardening. Moreover, in contrast with the isothermal case, the effective hardening rate increases when decreasing the initial temperature. The reason of this behavior can be found in the heat generation due to plastic dissipation. As it can be observed in Fig. 4(b) the temperature rise is higher for the lowest temperature due to the higher value of the strength (as it happened when analyzing the effect of loading direction). This temperature increase produces a softening of the material that is more evident for the lower initial temperature where the differences between isothermal and adiabatic cases are maximal. The resulting behavior is in agreement with the experimental observations showing a reduction of the strength for BCC Ta as a function of the initial temperature.

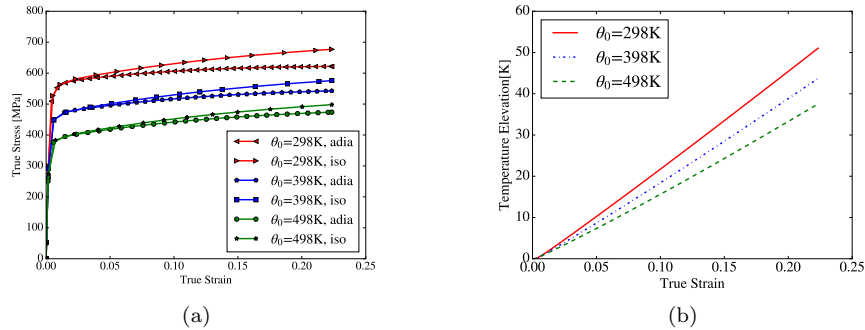


Figure 4: (a). Stress- (b). Temperature change-strain curves of BCC Ta during uniaxial traction at various initial temperatures

#### 4.3. Effects of strain rate

To study the effect of the strain rate on the material behavior of polycrystal Ta, the RVE is strained at three different engineering strain rates:  $5 \cdot 10^{-3}$ ,

5, and  $5 \cdot 10^3 \text{ s}^{-1}$ , all of them at 298K and under adiabatic conditions. The stress-strain response of the polycrystal for the three strain rates considered are plotted in Fig. 5(a). In this figure the effect of the strain rate can be clearly observed, the strength of the polycrystal increases when increasing the strain rate applied. These results are in quantitative agreement with the experimental results in [32]. The hardening effect is due to the elasto-visco-plastic nature of the CP selected and shows that increasing the strain rate is equivalent to reducing the temperature. The large differences found in the initial yield indicate a high strain rate sensitivity of the model for the energy parameters chosen even at room temperature. The effect of the strain rate in the thermal response of the polycrystal can be observed in Fig. 5(b) where the temperature increase is represented as a function of the applied strain for the three strain rates considered. The larger strain rates result in higher values of the effective strength and as a consequence the plastic dissipation increases and the temperature increases faster. It is interesting to note that the current framework is able to reproduce the analogous effect of decreasing the applied strain rate or increasing the initial temperature in both the mechanical response and in the temperature evolution.

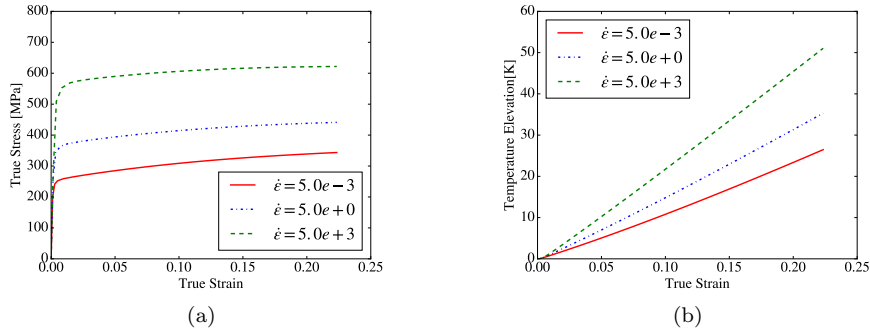


Figure 5: (a). Stress- (b). Temperature change-strain curves of BCC Ta during uniaxial traction tests at various engineering strain rates

#### 4.4. Effects of considering heat conduction at the microscale

Conventional approaches of thermo-mechanical coupled crystal plasticity often neglect the heat transfer. To study the effect of heat transfer on the responses of BCC Ta, comparative simulations were carried out to study the responses of the RVE during uniaxial traction tests, under macroscopic adiabatic conditions. Two different cases are considered, one where heat conduction at the microscale is considered and a second one where heat transfer is disabled also at the microscopic level. The maximum, minimum, and average value of the microscopic temperature field obtained for the three strain rates considered are given in Tab. 3. When heat diffusion is considered, it can be observed that for the two smallest strain rates, namely  $5\text{s}^{-1}$  and  $5 \cdot 10^{-3}\text{s}^{-1}$ , the temperature distribution on the microstructure is homogeneous. In contrast, when

	$\dot{\epsilon} = 5000 \text{ s}^{-1}$		$\dot{\epsilon} = 5 \text{ s}^{-1}$		$\dot{\epsilon} = 0.005 \text{ s}^{-1}$	
	No diff.	Full model	No diff.	Full model	No diff.	Full model
$T_{min}$ (K)	304.2	316.3	302.3	333.2	300.9	324.5
$T_{max}$ (K)	422.8	401.2	385.1	333.5	364.0	324.5
$T_{ave}$ (K)	349.1	349.1	333.2	333.3	324.4	324.5

Table 3: Maximum, minimum, and average local temperatures considering heat diffusion (full model) or a microscopic adiabatic condition (no diffusion)

microscopic heat conduction is not allowed (microscopic adiabatic condition), temperature distributions are heterogeneous and the differences between the maximum and minimum local temperatures are 80K and 63K, respectively, for the two strain rates. In contrast, for the highest strain rate ( $5 \cdot 10^3 \text{ s}^{-1}$ ) the full model with diffusion predicts an heterogeneous temperature distribution. This is an important result of the model because it shows that a characteristic time scale is introduced. Then, when strain rates are low, temperature becomes homogeneous, while for fast deformations the material behaves almost as microscopic-adiabatic.

To further analyze this behavior, the temperature field distribution at the end of the tensile simulation for the case at a nominal strain rate of  $5000 \text{ s}^{-1}$  is plotted in Fig. 6(a) for the case in which thermal conduction is considered and (b) for the microscopic-adiabatic case. Both figures show an heterogeneous distribution of the temperature due to the non-homogeneous distribution of the plastic deformation within the RVE. In both cases, the temperature hot-spots are the points in which plastic dissipation is maximum and correspond to the regions in which plastic strain is localized, near grain boundary or triple points. The comparison between the two figures suggests that the heat transfer plays a smoothing role, as expected. Allowing heat transfer at the microscale diffuses the temperature near the hottest points of the microstructure and the temperature gradients in Fig. 6(a) are reduced in comparison to the case without transfer, as shown in Fig. 6(b). This redistribution is very incipient here (time is  $5 \cdot 10^{-5} \text{ s}$ ) and temperature heterogeneities are still significant, but the heterogeneities disappear for larger times, as it happens at the end of the tests at  $5 \text{ s}^{-1}$  and  $5 \cdot 10^{-3} \text{ s}^{-1}$  (Tab 3).

#### 4.5. Comparison with Taylor homogenization model

To illustrate the difference between the results obtained using the full-field computational homogenization approach proposed in this work and the Taylor model, the cases studied in the previous sections are now simulated using this last approximation. In particular, the model was used to simulate uniaxial tensile tests performed at nominal strain rates of 0.005, 5.0 and  $5000 \text{ s}^{-1}$ , under both macroscopic adiabatic and isothermal conditions. The initial temperature was chosen to be 298 K in all cases.

The polycrystal was represented using 400 grains and the orientations of these grains were exactly the same as those in the RVE. The model parameters were

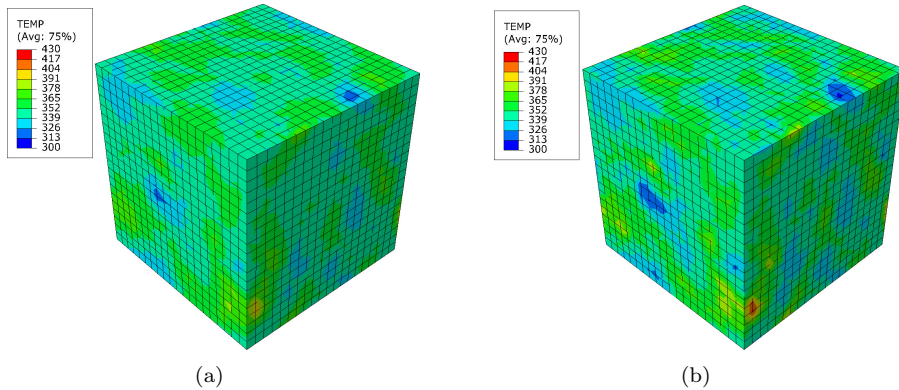


Figure 6: Temperature distributions of BCC Ta during uniaxial traction tests at  $\dot{\epsilon} = 5.0 \cdot 10^3 \text{ s}^{-1}$  under cases (a). with heat transfer and (b). without heat conduction

also the same as in previous simulations. The results under isothermal conditions are represented in Fig. 7. It can be observed that, for all the strain rates considered, the Taylor model produces a stiffer stress-strain response compared with the results obtained by the computational homogenization approach. The stiffer response of the Taylor model is well known and is due to the iso-strain assumption. This approach imposes that grains badly oriented for accommodating the plastic deformation deform identically to well oriented grains, artificially increasing their elastic strain level and therefore their contribution to the macroscopic stress. It must be noted that in the isothermal case the temperature does not play any role and the differences between (a), (b) and (c) are only due to the strain rate sensitivity of the crystal plasticity model.

The results obtained for macroscopic adiabatic conditions are represented in Fig. 8. It is shown that, similar to the isothermal case, under an adiabatic condition Taylor model still gives stiffer stress-strain response compared with the computational homogenization approach. However, the difference in strength between Taylor model and computational homogenization for this adiabatic condition is slightly smaller than the difference obtained under isothermal conditions. This small weakening of the Taylor model respect the computational homogeneization approach may be due to higher heat generated from overestimated stress response, which further produces a higher temperature and in return softens the stress response.

More interesting is the comparison of the temperatures obtained using the two homogenization approaches at the end of the simulation, and listed in Tab. 4. First, as pointed out in the previous section, it can be observed that allowing heat diffusion at the microscale influences the local temperature distribution. This re-distribution of temperature has an effect on the local behavior and therefore on the actual macroscopic response. In contrast with this effect, it can be observed that in the Taylor approach temperature differences persist for every strain rate. This is due to the grain-adiabatic condition used in the Taylor model

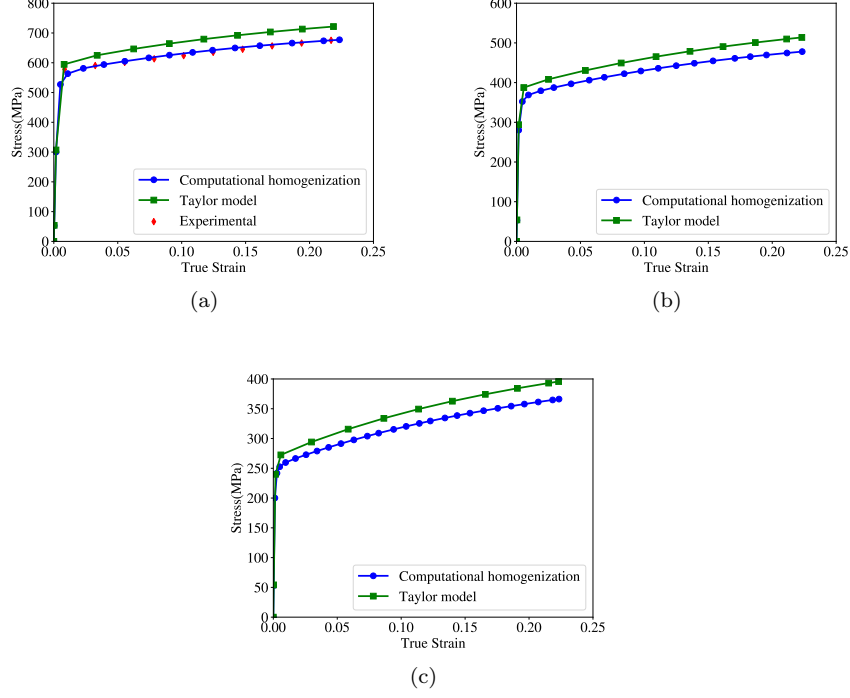


Figure 7: Comparison of stress-strain curves obtained by computational homogenization approach and Taylor model of BCC Ta during uniaxial tensile tests at various engineering strain rates and isothermal conditions. (a).  $\dot{\epsilon} = 5.0 \cdot 10^3 \text{ s}^{-1}$  (b).  $\dot{\epsilon} = 5.0 \text{ s}^{-1}$  (c).  $\dot{\epsilon} = 5.0 \cdot 10^{-3} \text{ s}^{-1}$

that does not allow heat redistribution within the grains, similarly to what happened when microscopic adiabatic condition was used in the computational model. In summary, the use of a Taylor approach results in a stiffer response and in a time-independent artificial temperature heterogeneity that might influence the mechanical results.

Table 4: Comparison of Temperature Distribution in Polycrystal Obtained by Taylor and Computational Homogenization

	$\dot{\epsilon} = 5000 \text{ s}^{-1}$		$\dot{\epsilon} = 5 \text{ s}^{-1}$		$\dot{\epsilon} = 0.005 \text{ s}^{-1}$	
	Taylor	Comp.	Taylor	Comp.	Taylor	Comp.
$T_{min}$ (K)	340.7	316.3	327.4	333.2	319.8	324.5
$T_{max}$ (K)	368.8	401.2	347.3	333.5	335.4	324.5
$T_{ave}$ (K)	353.8	349.1	336.7	333.3	327.2	324.5

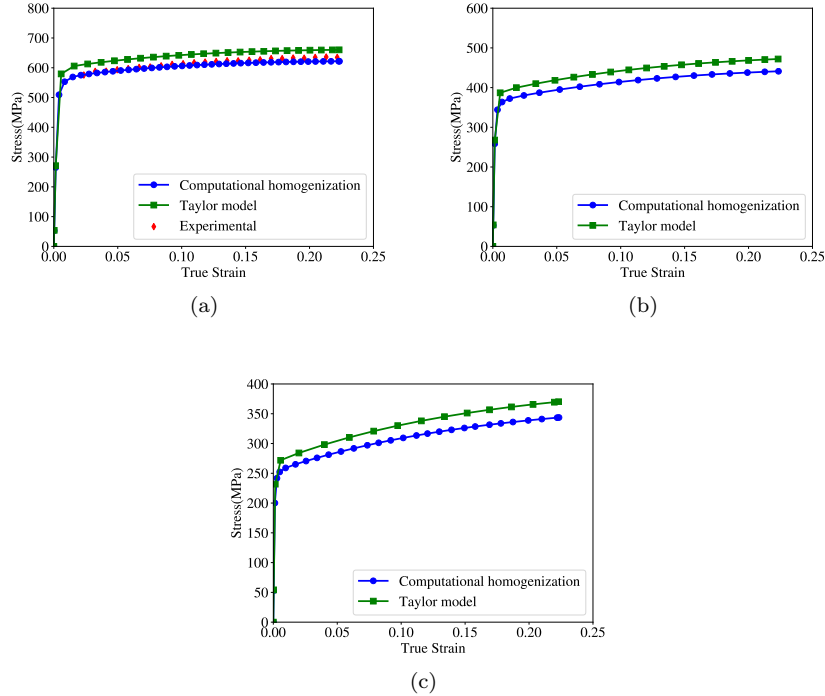


Figure 8: Comparison of stress-strain curves obtained by computational homogenization approach and Taylor model of BCC Ta during uniaxial tensile tests at various engineering strain rates and adiabatic conditions. (a).  $\dot{\epsilon} = 5.0 \cdot 10^{-3} \text{ s}^{-1}$  (c).  $\dot{\epsilon} = 5.0 \text{ s}^{-1}$  (e).  $\dot{\epsilon} = 5.0 \cdot 10^{-3} \text{ s}^{-1}$

## 5. Concluding Remarks

This work describes a thermo-mechanical crystal plasticity material model and its implementation in a thermo-mechanical finite element framework using strong field coupling and under finite strains. The model is used to obtain the response of a polycrystal by solving the thermo-mechanical problem on a periodic representative volume element of the microstructure.

The most relevant feature of the framework proposed is that, in contrast to phenomenological macroscopic approaches, the material response is based on the current physical mechanisms responsible of plastic deformation and is able to relate the macroscopic deformation with the crystallographic slip at the grain scale, including temperature and rate effects. Moreover, the numerical approach is able to resolve the heat diffusion at the microscale introducing an additional dependency of the macroscopic response with the strain rate, the lower the strain rate the closer to an isothermal state.

This two-scale approach for simulating thermo-mechanical processes can be used to provide enhanced predictions and understanding of the material behavior under extreme thermo-mechanical conditions, both at the macro and the

micro scales. The methods presented have been implemented into the commercial code ABAQUS through user-defined subroutines. The overall scheme has been employed in the solution of simple numerical examples which illustrate its general features and, in particular, its ability to capture the main coupling and hardening/softening effects observed in experiments.

### Acknowledgement

J. Li acknowledges the financial support from China Scholarship Council (Grant No. 201504890009). I. Romero and J. Segurado have been partially funded by projects DPI2015-67667-C3-1-R and DPI2015-67667-C3-2-R, respectively.

### References

#### References

- [1] G.R. Johnson and W.H. Cook. A constitutive model and data for metals subjected to large strains, high strain rates, and high temperatures. In *Proceedings of 7th International Symposium on Ballistics*, pages 541–547, 1983.
- [2] F.J. Zerilli and R.W. Armstrong. Dislocationmechanicsbased constitutive relations for material dynamics calculations. *Journal of Applied Physics*, 61(5):1816–1825, 1987.
- [3] P.S. Follansbee and U.F. Kocks. A constitutive description of the deformation of copper based on the use of the mechanical threshold stress as an internal state variable. *Acta Metallurgica*, 36(1):81 – 93, 1988.
- [4] R. Hill. Generalized constitutive relations for incremental deformation of metal crystals by multislip. *Journal of the Mechanics and Physics of Solids*, 14(2):95 – 102, 1966.
- [5] J.R. Rice. Inelastic constitutive relations for solids: An internal-variable theory and its application to metal plasticity. *Journal of the Mechanics and Physics of Solids*, 19(6):433 – 455, 1971.
- [6] R.J. Asaro and J.R. Rice. Strain localization in ductile single crystals. *Journal of the Mechanics and Physics of Solids*, 25(5):309 – 338, 1977.
- [7] D. Peirce, R.J. Asaro, and A. Needleman. Material rate dependence and localized deformation in crystalline solids. *Acta Metallurgica*, 31(12):1951 – 1976, 1983.
- [8] J. Segurado, R.A. Lebensohn, and J. Llorca. Computational homogenization of polycrystals. *Advances in Applied Mechanics*, 51:1–114, 04 2018.



- [9] A. Cruzado, B. Gan, M. Jimnez, D. Barba, K. Ostolaza, A. Linaza, J.M. Molina-Aldareguia, J. Llorca, and J. Segurado. Multiscale modeling of the mechanical behavior of IN718 superalloy based on micropillar compression and computational homogenization. *Acta Materialia*, 98:242 – 253, 2015.
- [10] C. Zhang, H. Li, P. Eisenlohr, W. Liu, C.J. Boehlert, M.A. Crimp, and T.R. Bieler. Effect of realistic 3d microstructure in crystal plasticity finite element analysis of polycrystalline Ti-5Al-2.5Sn. *International Journal of Plasticity*, 69:21 – 35, 2015.
- [11] V. Herrera-Solaz, J. LLorca, E. Dogan, I. Karaman, and J. Segurado. An inverse optimization strategy to determine single crystal mechanical behavior from polycrystal tests: Application to AZ31 Mg alloy. *International Journal of Plasticity*, 57:1 – 15, 2014.
- [12] G. Zhou, M.K. Jain, P. Wu, Y. Shao, D. Li, and Y. Peng. Experiment and crystal plasticity analysis on plastic deformation of az31b mg alloy sheet under intermediate temperatures: How deformation mechanisms evolve. *International Journal of Plasticity*, 79:19 – 47, 2016.
- [13] A. Shahba and S. Ghosh. Crystal plasticity FE modeling of Ti alloys for a range of strain-rates. Part I: A unified constitutive model and flow rule. *International Journal of Plasticity*, 87:48 – 68, 2016.
- [14] S. Ghosh, A. Shahba, X. Tu, E.L. Huskins, and B.E. Schuster. Crystal plasticity FE modeling of Ti alloys for a range of strain-rates. Part II: Image-based model with experimental validation. *International Journal of Plasticity*, 87:69 – 85, 2016.
- [15] R. Yuan, I.J. Beyerlein, and C. Zhou. Homogenization of plastic deformation in heterogeneous lamella structures. *Materials Research Letters*, 5(4):251–257, 2017.
- [16] J. Luo, G. Kang, and M. Shi. Simulation to the cyclic deformation of polycrystalline aluminum alloy using crystal plasticity finite element method. *International Journal of Computational Materials Science and Engineering*, 02:1350019, 2013.
- [17] W. Muhammad, A.P. Brahme, J. Kang, R.K. Mishra, and K. Inal. Experimental and numerical investigation of texture evolution and the effects of intragranular backstresses in aluminum alloys subjected to large strain cyclic deformation. *International Journal of Plasticity*, 93:137 – 163, 2017.
- [18] A. Cruzado, J. LLorca, and J. Segurado. Modeling cyclic deformation of inconel 718 superalloy by means of crystal plasticity and computational homogenization. *International Journal of Solids and Structures*, 122-123:148 – 161, 2017.

- [19] F.P.E. Dunne, D. Rugg, and A. Walker. Length scale-dependent, elastically anisotropic, physically-based hcp crystal plasticity: Application to cold-dwell fatigue in Ti alloys. *International Journal of Plasticity*, 23:1061 – 1083, 2007.
- [20] F. Bridier, D.L. McDowell, P. Villechaise, and J. Mendez. Crystal plasticity modeling of slip activity in ti6al4v under high cycle fatigue loading. *International Journal of Plasticity*, 25(6):1066 – 1082, 2009.
- [21] A. Rovinelli, M.D. Sangid, H. Proudhon, Y. Guilhem, R.A. Lebensohn, and W. Ludwig. Predicting the 3d fatigue crack growth rate of small cracks using multimodal data via bayesian networks: In-situ experiments and crystal plasticity simulations. *Journal of the Mechanics and Physics of Solids*, 115:208 – 229, 2018.
- [22] A. Cruzado, S. Lucarini, J. LLorca, and J. Segurado. Microstructure-based fatigue life model of metallic alloys with bilinear coffin-manson behavior. *International Journal of Fatigue*, 107:40 – 48, 2018.
- [23] B. Chen, J. Jiang, and F.P.E. Dunne. Is stored energy density the primary meso-scale mechanistic driver for fatigue crack nucleation? *International Journal of Plasticity*, 101:213 – 229, 2018.
- [24] G.B. Sarma and B. Radhakrishnan. Modeling microstructural effects on the evolution of cube texture during hot deformation of aluminum. *Materials Science and Engineering: A*, 385(1):91 – 104, 2004.
- [25] T. Walde and H. Riedel. Modeling texture evolution during hot rolling of magnesium alloy az31. *Materials Science and Engineering: A*, 443(1-2):277 – 284, 2007.
- [26] J.R. Mayeur, I.J. Beyerlein, C.A. Bronkhorst, and H.M. Mourad. Incorporating interface affected zones into crystal plasticity. *International Journal of Plasticity*, 65:206 – 225, 2015.
- [27] A. Gupta, M.B. Bettaieb, F. Abed-Meraim, and S.R. Kalidindi. Computationally efficient predictions of crystal plasticity based forming limit diagrams using a spectral database. *International Journal of Plasticity*, 103:168 – 187, 2018.
- [28] I.J. Beyerlein and C.N. Tomé. A dislocation-based constitutive law for pure zr including temperature effects. *International Journal of Plasticity*, 24(5):867 – 895, 2008.
- [29] K.S. Cheong, E.P. Busso, and A. Arsenlis. A study of microstructural length scale effects on the behaviour of fcc polycrystals using strain gradient concepts. *International Journal of Plasticity*, 21:1797 – 1814, 2005.

- [30] D. Rodriguez-Galn, I. Sabirov, and J. Segurado. Temperature and strain rate effect on the deformation of nanostructured pure titanium. *International Journal of Plasticity*, 70:191–205, 2015.
- [31] P. Hu, Y. Liu, Y. Zhu, and L. Ying. Crystal plasticity extended models based on thermal mechanism and damage functions: Application to multiscale modeling of aluminum alloy tensile behavior. *International Journal of Plasticity*, 86:1 – 25, 2016.
- [32] M. Kothari and L. Anand. Elasto-viscoplastic constitutive equations for polycrystalline metals: Application to tantalum. *Journal of the Mechanics and Physics of Solids*, 46(1):51 – 83, 1998.
- [33] P. Hakansson, M.Wallin, and M. Ristinmaa. Prediction of stored energy in polycrystalline materials during cyclic loading. *International Journal of Solids and Structures*, 45(6):1570 – 1586, 2008.
- [34] J. Rossiter, A. Brahme, M.H. Simha, K. Inal, and R. Mishra. A new crystal plasticity scheme for explicit time integration codes to simulate deformation in 3d microstructures: Effects of strain path, strain rate and thermal softening on localized deformation in the aluminum alloy 5754 during simple shear. *International Journal of Plasticity*, 26(12):1702 – 1725, 2010.
- [35] S. Bargmann and M. Ekh. Microscopic temperature field prediction during adiabatic loading using gradient extended crystal plasticity. *International Journal of Solids and Structures*, 50(6):899 – 906, 2013.
- [36] R. Seghir, E. Charkaluk, P. Dufrenoy, and L. Bodelot. Thermomechanical couplings in crystalline plasticity under fatigue loading. *Procedia Engineering*, 2(1):1155 – 1164, 2010. Fatigue 2010.
- [37] E.D. Cyr, M. Mohammadi, R.K. Mishra, and K. Inal. A three dimensional (3d) thermo-elasto-viscoplastic constitutive model for fcc polycrystals. *International Journal of Plasticity*, 70:166 – 190, 2015.
- [38] A.A. Benzerga, Y. Brechet, A. Needleman, and E. Van der Giessen. The stored energy of cold work: Predictions from discrete dislocation plasticity. *Acta Materialia*, 53(18):4765 – 4779, 2005.
- [39] E.H. Lee and D.T. Liu. Finitestrain elasticplastic theory with application to planewave analysis. *Journal of Applied Physics*, 38(1):19–27, 1967.
- [40] F.T. Meissonnier, E.P. Busso, and N.P. O’Dowd. Finite element implementation of a generalised non-local rate-dependent crystallographic formulation for finite strains. *International Journal of Plasticity*, 17(4):601 – 640, 2001.
- [41] R.J. Asaro and A. Needleman. Texture development and strain hardening in rate dependent polycrystals. *Acta Metallurgica*, 33(6):923 – 953, 1985.

- [42] H.J. Frost and M.F. Ashby. *Deformation Mechanism Maps: the plasticity and creep of metals and ceramics*. Pergamon Press, 1982.
- [43] D. Peirce, R.J. Asaro, and A. Needleman. An analysis of nonuniform and localized deformation in ductile single crystals. *Acta Metallurgica*, 30(6):1087 – 1119, 1982.
- [44] S.B. Brown, K.H. Kim, and L. Anand. An internal variable constitutive model for hot working of metals. *International Journal of Plasticity*, 5(2):95 – 130, 1989.
- [45] A. Cottrell and R. Stokes. Effects of temperature on the plastic properties of aluminium crystals. *Proceedings of the Royal Society of London A: Mathematical, Physical and Engineering Sciences*, 233(1192):17–34, 1955.
- [46] G.I. Taylor. Plastic strain in metals. *Journal of the Institute of Metals*, 62:307–324, 1938.
- [47] A. Molinari, G.R. Canova, and S. Ahzi. A self consistent approach of the large deformation polycrystal viscoplasticity. *Acta Metallurgica*, 35(12):2983 – 2994, 1987.
- [48] R.A. Lebensohn and C.N. Tomé. A self-consistent anisotropic approach for the simulation of plastic deformation and texture development of polycrystals: Application to zirconium alloys. *Acta Metallurgica et Materialia*, 41(9):2611 – 2624, 1993.
- [49] C.N. Tomé and R.A. Lebensohn. *Self Consistent Homogenization Methods for Texture and Anisotropy*, chapter 23, pages 473–499. Wiley-Blackwell, 2005.
- [50] J. Segurado, R.A. Lebensohn, J. LLorca, and C.N. Tomé. Multiscale modeling of plasticity based on embedding the viscoplastic self-consistent formulation in implicit finite elements. *International Journal of Plasticity*, 28(1):124 – 140, 2012.
- [51] F. Roters, P. Eisenlohr, T.R. Bieler, and D. Raabe. *Homogenization*, chapter 7, pages 93–108. Wiley-Blackwell, 2010.
- [52] H.J. Böhm. *A Short Introduction to Continuum Micromechanics*. Springer-Verlag Wien, 2004.
- [53] J. Segurado and J. Llorca. Simulation of the deformation of polycrystalline nanostructured Ti by computational homogenization. *Computational Materials Science*, 76:3 – 11, 2013.
- [54] G. Simmons and H. Wang. *Single Crystal Elastic Constants and Calculated Aggregate Properties: A Handbook*. The MIT Press, Cambridge, 1971.
- [55] S. Nemat-Nasser and J.B. Isaacs. Direct measurement of isothermal flow stress of metals at elevated temperatures and high strain rates with application to ta and taw alloys. *Acta Materialia*, 45(3):907 – 919, 1997.